The Astronomical Journal, 165:41 (9pp), 2023 February https://doi.org/10.3847/1538-3881/aca277
© 2023. The Author(s). Published by the American Astronomical Society.
OPEN ACCESS

Simultaneous Six-way Observations from the Navy Precision Optical Interferometer

Ellyn K. Baines[1], Solvay Blomquist[2], James H. Clark III[1], Jim Gorney[2], Erin Maier[2], Jason Sanborn[2], Henrique R. Schmitt[1], Jordan M. Stone[1], Gerard T. van Belle[2], and Kaspar von Braun[2]
[1] Naval Research Laboratory, Remote Sensing Division, 4555 Overlook Ave SW, Washington, DC 20375, USA
[2] Lowell Observatory, 1400 W. Mars Hill Rd, Flagstaff, AZ 86001, USA; ellyn.baines@nrl.navy.mil
Received 2022 September 21; revised 2022 October 27; accepted 2022 November 9; published 2023 January 9

Abstract

We measured the angular diameters of six stars using the six-element observing mode of the Navy Precision Optical Interferometer (NPOI) for the first time since the early 2000s. Four of the diameters ranged from 1.2 to 1.9 mas, while the two others were much smaller at approximately 0.5 mas to 0.7 mas, which are the two smallest angular diameters measured to date with the NPOI. There is a larger spread in the measurements than data obtained with three-, four-, or five-element modes, which can be attributed in part to the flux imbalance due to the combination of more than two siderostats in a single spectrograph, and also to crosstalk between multiple baselines related to nonlinearities in the fast-delay-line dither strokes. We plan to address this in the future by using the VISION beam combiner.

Unified Astronomy Thesaurus concepts: Fundamental parameters of stars (555); High angular resolution (2167); Optical interferometry (1168)

1. Introduction

The Navy Precision Optical Interferometer (NPOI) has been in operation since 1994, originally with the name Navy Prototype Optical Interferometer and then, briefly, Navy Optical Interferometer. It is a Y-shaped optical interferometer located on Anderson Mesa near Flagstaff, AZ. The NPOI was originally designed to combine light from six elements[3] as a balance between financial cost, instrument complexity, and the tension between a philosophy of "if some is good, more is better" and the dilution of fringes across multiple apertures (Armstrong et al. 1998).

The NPOI consists of two nested subarrays that can be combined at will, depending on the requirements for specific scientific questions. The four stations of the astrometric array are fixed near the center of the Y, and are named AC, AE, AN, and AW, which stand for astrometric center, east, north, and west, respectively. The other subarray is the imaging array spread along the three north-, east-, and west-oriented arms of the NPOI. Each arm has ten piers on which a siderostat can be placed, meaning the imaging array can be reconfigured as needed. The stations are labeled according to which arm they are on and how far away they are from the array center, with 1 being closest and 10 being farthest away. This paper includes data from AC, AE, and AW of the astrometric array, and E6, W4, and W7 of the imaging array.

The NPOI has used many different configurations through the years, from a single baseline (i.e., two imaging elements where the "baseline" is the distance between them) up to six-way beam combination. Most of the time, the NPOI has used three to five siderostats at a time, which has the advantage of increasing sky coverage and the length of time a given target is observable as it moves through the available swath of sky. The NPOI first went on-sky in six-way mode in 2001 September during on-sky tests, and routine observations began 2002 January (Benson et al. 2003). Results from that time include imaging the triple star η Virginis, modeling its orbit and detecting the motion of the close pair over time (Hummel et al. 2003). Six-way mode was suspended not long afterwards when other observational programs took precedence, and chronic problems with delay lines made this type of operation impractical.

One of the main issues that led to halting six-way data collection at that time was the reduced sky coverage that can be achieved in six-way when one uses the longest baselines without the long delay lines, usually of the order of 1 hour or less over a narrow range of declinations. The other more severe issue was the irregularities in the fast-delay-line (FDL) strokes and their truncated range of motion for the largest stroke amplitude of 4 μm (Jorgensen et al. 2006), which resulted in crosstalk between baselines with adjacent stroke frequencies. In addition to these issues, one of the delay lines was taken offline for an extended period of time in order to develop new FDL controllers. Although we were not able to address issues related limited sky coverage and stroke irregularities when returning to six-way observing in 2021, we avoided the truncated range of motion issue by using only stroke amplitudes up to ± 3 μm.

This paper is organized as follows. Section 2 outlines our observing and data reduction procedures. Section 3 describes how we determined various stellar parameters such as angular diameters, physical radii, effective temperatures, bolometric flux, and luminosity. Section 4 presents notes on individual fits, when applicable, and plans for future six-way observations.

2. Interferometric Observations

We observed six stars in six-way mode in 2021 August and September, collecting nearly 23,000 calibrated data points. The stars were selected to be small ($\leqslant$2.0 mas) and bright ($V \leqslant 4.3$) so that finding interferometric fringes on all tracking baselines would not present an undue challenge. Table 1 lists each star's

[3] The NPOI observes with siderostats, and in this paper "six-way observing" means we observed using six siderostats simultaneously.

Original content from this work may be used under the terms of the Creative Commons Attribution 4.0 licence. Any further distribution of this work must maintain attribution to the author(s) and the title of the work, journal citation and DOI.

Table 1
Sample Star Properties

HD	HR	FK5	Other Name	Spectral Type	V (mag)	Parallax (mas)	References	[Fe/H]
6186	294	36	ϵ Psc	G9III	4.27	17.81	1	−0.29
10761	510	60	o Psc	G8III	4.26	12.53	1	−0.03
182640	7377	730	δ Aql	F1IV-V	3.36	64.41	2	−0.04
187929	7570	746	η Aql	F6I+B9.8V	3.73	2.61	3	0.13
198001	7950	781	ϵ Aqr	B9.5V	3.77	13.36	1	−0.31
210418	8450	834	θ Peg	A1V	3.52	36.77	3	−0.38

Note. Spectral types are from SIMBAD; V magnitudes are from Mermilliod (2006); parallaxes are from the following sources: Gaia DR3 (Gaia Collaboration et al. 2023), van Leeuwen (2007), Gaia Collaboration et al. (2018); and [Fe/H] is from Anderson & Francis (2012).

Table 2
Observing Log

Target HD	Calibrator HD	Date (UT)	Baselines Used	# Data Points
6186	886	24 Aug 2021	AC-AE, AC-AW, AC-E6, AC-W4, AC-W7, AE-AW, AE-W7, AW-E6, AW-W4, E6-W4	96
		25 Aug 2021	AC-AE, AC-AW, AC-E6, AC-W4, AC-W7, AE-AW, AE-W7, AW-E6, AW-W4, AW-W7, E6-W4	480
		5 Sep 2021	AC-AE, AC-AW, AC-E6, AC-W4, AC-W7, AE-AW, AE-W7, AW-E6, AW-W4, AW-W7, E6-W4	630
		8 Sep 2021	AC-AE, AC-AW, AC-E6, AC-W4, AC-W7, AE-AW, AE-W7, AW-E6, AW-W4, AW-W7, E6-W4	960
		11 Sep 2021	AC-AE, AC-AW, AC-E6, AC-W4, AC-W7, AE-AW, AE-W7, AW-E6, AW-W4, AW-W7, E6-W4	220
		12 Sep 2021	AC-AE, AC-AW, AC-E6, AC-W4, AC-W7, AE-AW, AE-W7, AW-E6, AW-W4, AW-W7, E6-W4	470
		16 Sep 2021	AC-AE, AC-AW, AC-E6, AC-W4, AC-W7, AE-AW, AE-W7, AW-E6, AW-W4, AW-W7, E6-W4	540
10761	16582	5 Sep 2021	AC-AE, AC-AW, AC-E6, AC-W4, AC-W7, AE-AW, AE-W7, AW-E6, AW-W4, AW-W7, E6-W4	950
		7 Sep 2021	AC-AE, AC-AW, AC-E6, AC-W4, AC-W7, AE-AW, AE-W7, AW-E6, AW-W4, AW-W7, E6-W4	360
		11 Sep 2021	AC-AE, AC-AW, AC-W4, AC-W7, AE-AW, AE-W7, AW-W4, AW-W7	180
		12 Sep 2021	AC-AE, AC-AW, AC-E6, AC-W4, AC-W7, AE-AW, AE-W7, AW-E6, AW-W4, AW-W7, E6-W4	580
		16 Sep 2021	AC-AE, AC-AW, AC-E6, AC-W4, AC-W7, AE-AW, AE-W7, AW-E6, AW-W4, AW-W7, E6-W4	450
182640	177756	13 Jun 2021	AC-AE, AC-E6, AC-W4, E6-W4	530
		14 Jun 2021	AC-AE, AC-E6, AC-W4, E6-W4	490
		25 Aug 2021	AC-AE, AC-AW, AC-E6, AC-W4, AC-W7, AE-AW, AE-W7, AW-W4, AW-W7, E6-W4	555
		27 Aug 2021	AC-AE, AC-AW, AC-E6, AC-W4, AC-W7, AE-AW, AE-W7, AW-E6, AW-W4, AW-W7, E6-W4	1540
		28 Aug 2021	AC-AE, AC-AW, AC-E6, AC-W4, AC-W7, AE-AW, AE-W7, AW-E6, AW-W4, AW-W7, E6-W4	660
		5 Sep 2021	AC-AE, AC-AW, AC-W4, AC-W7, AE-AW, AE-W7, AW-E6, AW-W4, AW-W7	558
		6 Sep 2021	AC-AE, AC-AW, AC-E6, AC-W4, AC-W7, AE-AW, AE-W7, AW-E6, AW-W4, AW-W7, E6-W4	2379
		8 Sep 2021	AC-AE, AC-AW, AC-E6, AC-W4, AC-W7, AE-AW, AE-W7, AW-E6, AW-W4, AW-W7, E6-W4	850
		9 Sep 2021	AC-AE, AC-AW, AC-E6, AC-W4, AC-W7, AE-AW, AE-W7, AW-E6, AW-W4, AW-W7, E6-W4	1477
		12 Sep 2021	AC-AE, AC-AW, AC-E6, AC-W4, AC-W7, AE-AW, AE-W7, AW-E6, AW-W4, AW-W7	599
		16 Sep 2021	AC-AE, AC-AW, AC-W7, AE-AW, AE-W7, AW-W7	60
187929	184930	25 Aug 2021	AC-AE, AC-AW, AC-E6, AC-W4, AC-W7, AE-AW, AE-W7, AW-E6, AW-W4, AW-W7, E6-W4	996
198001	200761	5 Sep 2021	AC-AE, AC-AW, AC-E6, AC-W4, AC-W7, AE-AW, AE-W7, AW-E6, AW-W4, AW-W7, E6-W4	1780
		6 Sep 2021	AC-AE, AC-AW, AC-E6, AC-W4, AC-W7, AE-AW, AE-W7, AW-E6, AW-W4, AW-W7, E6-W4	360
		12 Sep 2021	AC-AE, AC-AW, AC-E6, AC-W4, AC-W7, AE-AW, AE-W7, AW-E6, AW-W4, AW-W7, E6-W4	480
		16 Sep 2021	AC-AE, AC-AW, AC-E6, AC-W4, AC-W7, AE-AW, AE-W7, AW-E6, AW-W4, AW-W7, E6-W4	510
210418	214923	24 Aug 2021	AC-AE, AC-AW, AC-E6, AC-W4, AC-W7, AE-AW, AE-W7, AW-E6, AW-W4, E6-W4	655
		27 Aug 2021	AC-AE, AC-AW, AC-E6, AC-W4, AC-W7, AE-AW, AE-W7, AW-E6, AW-W4, AW-W7, E6-W4	840
		5 Sep 2021	AC-AE, AC-AW, AC-E6, AC-W4, AC-W7, AE-AW, AE-W7, AW-E6, AW-W4, AW-W7, E6-W4	840
		8 Sep 2021	AC-AE, AC-AW, AC-W7, AE-AW, AE-W7, AW-W7	381
		11 Sep 2021	AC-AE, AC-AW, AC-W4, AC-W7, AE-AW, AE-W7, AW-W4, AW-W7	90
		12 Sep 2021	AC-AE, AC-AW, AC-E6, AC-W4, AC-W7, AE-AW, AE-W7, AW-E6, AW-W4, AW-W7, E6-W4	720

Note. See Table 3 for the baseline lengths, and Figure 1 for a representation of the configuration used.

identifiers, spectral type, V magnitude, parallax, and metallicity. Table 2 is the observing log and includes the stars observed, their calibrators, dates, the baselines used, and number of data points per night (note that one of the stars also includes five-way data taken in 2021 June). We used the "Classic" beam combiner (Hummel et al. 2003; Benson et al. 2003; Hutter et al. 2016) that takes data across 16 spectral channels in the visible regime from 550 nm to 850 nm.

Hardware limitations prevent us from recording all 15 baselines possible with the six imaging elements, so these types of observations produce fringes on 11 simultaneous baselines. This is because we use two spectrographs with four siderostats on each, giving us six baselines per spectrograph. One of those baselines is repeated on each spectrograph, which is how we end up with 11 baselines per observation. Table 3 shows a list of the baselines used, and Figure 1 shows the configuration.

Table 3
Baselines

Baseline	Length (m)
Spectrograph 1	
AC-AE	18.9
AC-AW	22.2
AC-W7	51.6
AE-AW	44.1
AE-W7	64.4
AW-W7	29.5
Spectrograph 2	
AC-AW	22.2
AC-E6	34.3
AC-W4	8.8
AW-E6	53.3
AW-W4	14.0
E6-W4	42.5

We interleaved scans on the target stars with scans of calibrator stars to help minimize errors introduced by atmospheric turbulence and instrumental imperfections. We chose calibrator stars with small angular diameters[4] and checked for binarity, variability, and rapid rotation. Some of the calibrator stars used featured one or more of those characteristics, but not to an extent that would affect the calibration process: any binary separations or brightness ratios were beyond the detection limit of the configuration used, while oblateness due to rapid rotation and/or variability did not introduce a variation in the diameter of the star that would be large enough to cause significant calibration issues.

To estimate the calibrator stars' angular diameters, we created spectral energy distribution (SED) fits based on published *UBVRIJHK* photometric values. We used plane-parallel model atmospheres (Castelli & Kurucz 2003) based on effective temperature ($T_{\rm eff}$), surface gravity ($\log g$), and E ($B-V$). Stellar models were fit to observed photometry after converting the magnitudes to fluxes using Colina et al. (1996) for *UBVRI* and Cohen et al. (2003) for *JHK*. Table 4 lists the photometry, $T_{\rm eff}$, $\log g$, and $E(B-V)$ used, and the resulting angular diameters. This is a simple SED fit, unlike the more sophisticated one described in Section 3.2 that we used for the target stars. It is an appropriate method for calibrator stars, given the insensitivity of the target's measured angular diameter with respect to the calibrator's diameter (Baines et al. 2018).

Each observation consisted of a 30 s coherent (on the fringe) scan where the fringe contrast was measured every 2 ms. Every coherent scan was paired with an incoherent (off the fringe) scan, which acted as an estimate for the additive bias affecting fringe measurements (Hummel et al. 2003). Each coherent scan was averaged to 1 s data points, and then again to a single 30 s average. The dispersion of the 1 s data points served as an estimate of the internal uncertainties. The NPOI's data reduction package *OYSTER* was developed by C. A. Hummel[5] and automatically edits data using the method described in Hummel et al. (2003).

In addition to the automated process, we edited out individual data points and/or scans that showed large scatter, on the order of 5σ or higher. This was more common in the channels corresponding to shorter wavelengths where the spectral channels are narrower, atmospheric effects are more pronounced, and the avalanche photodiode detectors have lower quantum efficiency. Removing these points did not affect the diameter measurements.

3. Determining Stellar Parameters

3.1. Angular Diameter Measurement

Interferometric diameter measurements use visibility squared (V^2). For a point source, V^2 is 1 and it is considered completely

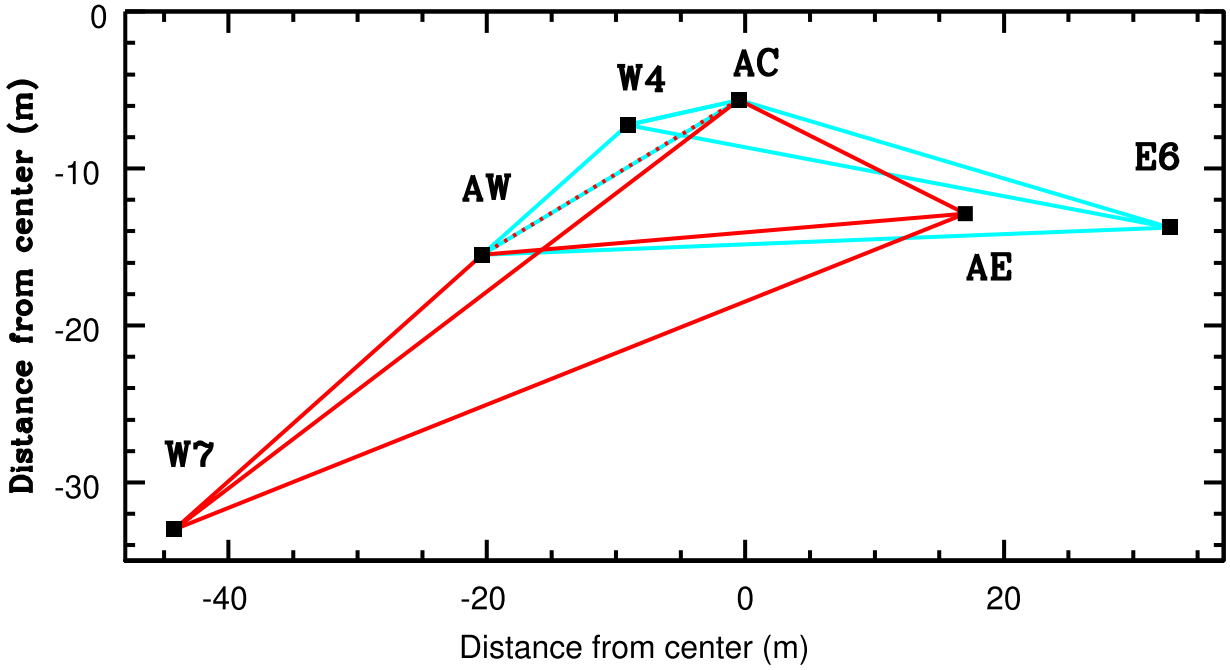

Figure 1. The NPOI configuration used for six-way observing. The squares show the locations of the siderostats as a function of distance from the center, the red lines show the baselines on spectrograph 1, and the blue lines show the baselines on spectrograph 2. The dashed line is the baseline that repeats on both spectrographs. Table 3 lists the lengths of the various baselines.

Table 4
Calibrator Stars' SED Inputs and Angular Diameters

HD	Spec Type	U (mag)	B (mag)	V (mag)	R (mag)	I (mag)	J (mag)	H (mag)	K (mag)	$T_{\rm eff}$ (K)	log g (cm s^{-2})	Ref	$E(B-V)$	Referances	$\theta_{\rm est}$ (mas)
886	B2IV	1.75	2.61	2.83	2.88	3.06	3.50	3.64	3.77	21944	3.93	1	0.02	4	0.45 ± 0.02
16582	B2IV	3.00	3.85	4.07	4.15	4.34	4.80	4.74	4.70	24118	4.19	2	0.00	5	0.23 ± 0.01
177756	B8.5V	3.07	3.34	3.43	3.44	3.52	3.52	3.48	3.56	11749	4.22	3	0.00	6	0.56 ± 0.03
184930	B5III	3.84	4.28	4.36	4.37	4.46	4.44	4.42	4.48	10471	3.72	3	0.07	7	0.45 ± 0.02
200761	A1V	4.06	4.05	4.06	4.07	4.09	4.37	4.32	4.10	9550	4.01	3	0.01	8	0.50 ± 0.03
214923	B8V	3.10	3.32	3.41	3.43	3.51	3.54	3.53	3.57	10965	3.75	3	0.01	9	0.60 ± 0.03

Note. Spectral types are from SIMBAD; *UBV* values are from Mermilliod (2006); *RI* values are from Monet et al. (2003); *JHK* values are from Cutri et al. (2003); $T_{\rm eff}$, log g, and $E(B-V)$ values are from the following sources: Prugniel et al. (2007), McDonald et al. (2017), Allende Prieto & Lambert (1999), Sánchez-Blázquez et al. (2006), Gaia DR3 (Gaia Collaboration et al. 2023), Alonso et al. (1996), Wegner (2003), Neckel et al. (1980), and Zorec et al. (2009); $\theta_{\rm est}$ is the estimated angular diameter calculated using the method described in Section 2.

Table 5
Interferometric Results

Target HD	θ_{UD} (mas)	T_{eff} (K)	log g (cm s^{-2})	Ref	Initial μ_λ	$\theta_{LD,initial}$ (mas)	Final μ_λ	$\theta_{LD,final}$ (mas)	σ_{LD} (%)	Max SF (10^6 cycles s^{-1})	# pts
6186	1.813 ± 0.025	4898	2.59	1	0.64	1.885 ± 0.025	0.65	1.887 ± 0.025	1.3	98.0	3396
10761	1.583 ± 0.018	5026	2.52	2	0.65	1.679 ± 0.018	0.64	1.677 ± 0.018	1.1	97.6	2520
182640	1.163 ± 0.016	7413	4.21	1	0.45	1.199 ± 0.016	0.48	1.203 ± 0.016	1.3	114.5	9698
187929	1.713 ± 0.055	5808	1.84	2	0.56	1.808 ± 0.055	0.56	1.808 ± 0.055	3.0	111.8	996
198001	0.434 ± 0.357	9120	3.55	1	0.42	0.504 ± 0.357	0.39	0.503 ± 0.357	71.0	95.6	3130
210418	0.643 ± 0.031	8511	4.02	1	0.45	0.689 ± 0.031	0.43	0.688 ± 0.031	4.5	97.4	3526

Note. The initial μ_λ is based on the T_{eff} and log g listed in the table, and the final μ_λ is based on the new T_{eff} determination. (See Section 3.2 for more details). The T_{eff} and log g are from the following sources: Allende Prieto & Lambert (1999) and Gaia DR3 (Gaia Collaboration et al. 2023). Max SF is the maximum spatial frequency for that star's diameter measurement. # pts is the number of data points in the angular diameter fit.

unresolved, while a star is defined as completely resolved when its V^2 reaches zero. For a uniformly-illuminated disk, $V^2 = [2J_1(x)/x]^2$, where J_1 is the Bessel function of the first order, $x = \pi B \theta_{UD} \lambda^{-1}$, B is the projected baseline toward the star's position, θ_{UD} is the apparent uniform disk angular diameter of the star, and λ is the effective wavelength of the observation (Shao & Colavita 1992). θ_{UD} results for our program stars are listed in Table 5, and the data are freely available in OIFITS form (Duvert et al. 2017) upon request.

A more realistic description of a star's surface brightness includes limb darkening (LD). If a linear LD coefficient μ_λ is used, then

$$V^2 = \left(\frac{1-\mu_\lambda}{2} + \frac{\mu_\lambda}{3}\right)^{-1} \times \left[(1-\mu_\lambda)\frac{J_1(x_{LD})}{x_{LD}} + \mu_\lambda\left(\frac{\pi}{2}\right)^{1/2}\frac{J_{3/2}(x_{LD})}{x_{LD}^{3/2}}\right]^2, \quad (1)$$

where $x_{LD} = \pi B \theta_{LD} \lambda^{-1}$ (Hanbury Brown et al. 1974). We used T_{eff}, log g, and metallicity ([Fe/H]) values from the literature with an assumed microturbulent velocity of 2 km s^{-1} to obtain μ_λ from Claret & Bloemen (2011). We used the ATLAS stellar model in the R-band, the wave band most closely matched to the central wavelength of the NPOI's bandpass. A more sophisticated analysis of these stars would include the nonlinear nature of LD, and how it depends on wavelength. The simpler treatment here is valid, given that the strength of the LD for the star is related to the height of the second maximum of the visibility curve (Wittkowski et al. 2001), and none of our measurements were beyond the first minimum.

The T_{eff}, log g, and μ_λ used and the resulting limb-darkened diameters (θ_{LD}) are listed in Table 5 along with the maximum spatial frequency for each star's data set, and the number of data points in the angular diameter fit. Figure 2 shows the θ_{LD} fits for the six stars.

We used the procedure described in Baines et al. (2018) to estimate angular diameter uncertainties, which can be summarized thus: if we fit only the collected data points without regard to correlations within a scan, the diameter's uncertainty can be significantly underestimated. To address this, we used a modified bootstrap Monte Carlo method developed by Tycner et al. (2010) to generate a large number of synthetic data sets by randomly selecting entire scans. The width of the distribution of diameters fit to these data sets becomes our measure of the uncertainty for the diameter (see Figure 3).

3.2. Stellar Radius, Luminosity, and Effective Temperature

Our next step was to convert our angular diameters to stellar sizes in solar radii. When available, the parallax from the Gaia Data Release 3 (Gaia Collaboration et al. 2023) was converted into a distance and combined with our measured diameters to calculate the physical radius R. Otherwise, parallaxes from van Leeuwen (2007) and Gaia Collaboration et al. (2018) were used.

In order to determine each star's luminosity (L) and T_{eff}, we generated SED fits using photometric values published in Johnson et al. (1966), Golay (1972), Johnson & Mitchell (1975), Oja (1984), Mermilliod (1987), Helou & Walker (1988), Beichman et al. (1988), Mermilliod & Nitschelm (1989), Mermilliod (2006), Gezari et al. (1993), Oja (1993), Gezari et al. (1999), Høg et al. (2000), Ducati (2002), Cutri et al. (2003), Smith et al. (2004), and van Leeuwen (2007). The assigned uncertainties for the 2MASS infrared measurements are as reported in Cutri et al. (2003), and an uncertainty of 0.05 mag was assigned to the optical measurements.

Spectrophotometry from Burnashev (1996), Glushneva et al. (1983), and Kharitonov et al. (1988) were included for HD 6186/ϵ Psc, HD 10761/o Psc, HD 182640/δ Aql, but not HD 198001/ϵ Aqr and HD 210418/θ Peg. HD 187929/η Aql is a well-known Cepheid variable, and the SED fit did not produce usable results so the remainder of the following calculations apply to the remaining five stars.

We determined the best-fit stellar spectral template to the photometry and spectrophotometry, if used, from the flux-calibrated stellar spectral atlas of Pickles (1998) using the χ^2 minimization technique (Press et al. 1992; Wall & Jenkins 2003). This provided the bolometric flux (F_{BOL}) for each star and allowed for the calculation of extinction (A_V) with the wavelength-dependent reddening relations of Cardelli et al. (1989).

We combined our F_{BOL} values with the stars' distances to estimate L using $L = 4\pi d^2 F_{BOL}$. We also combined the F_{BOL} with θ_{LD} to determine each star's T_{eff} using the relation,

$$F_{BOL} = \frac{1}{4}\theta_{LD}^2 \sigma T_{eff}^4, \quad (2)$$

where σ is the Stefan-Boltzmann constant and θ_{LD} is in radians (van Belle et al. 1999). The resulting R, F_{BOL}, A_V, T_{eff}, and L are listed in Table 6.

[4] Here, "small" means that the star's diameter is significantly less than the resolution of the interferometer.
[5] www.eso.org/~chummel/oyster/oyster.html

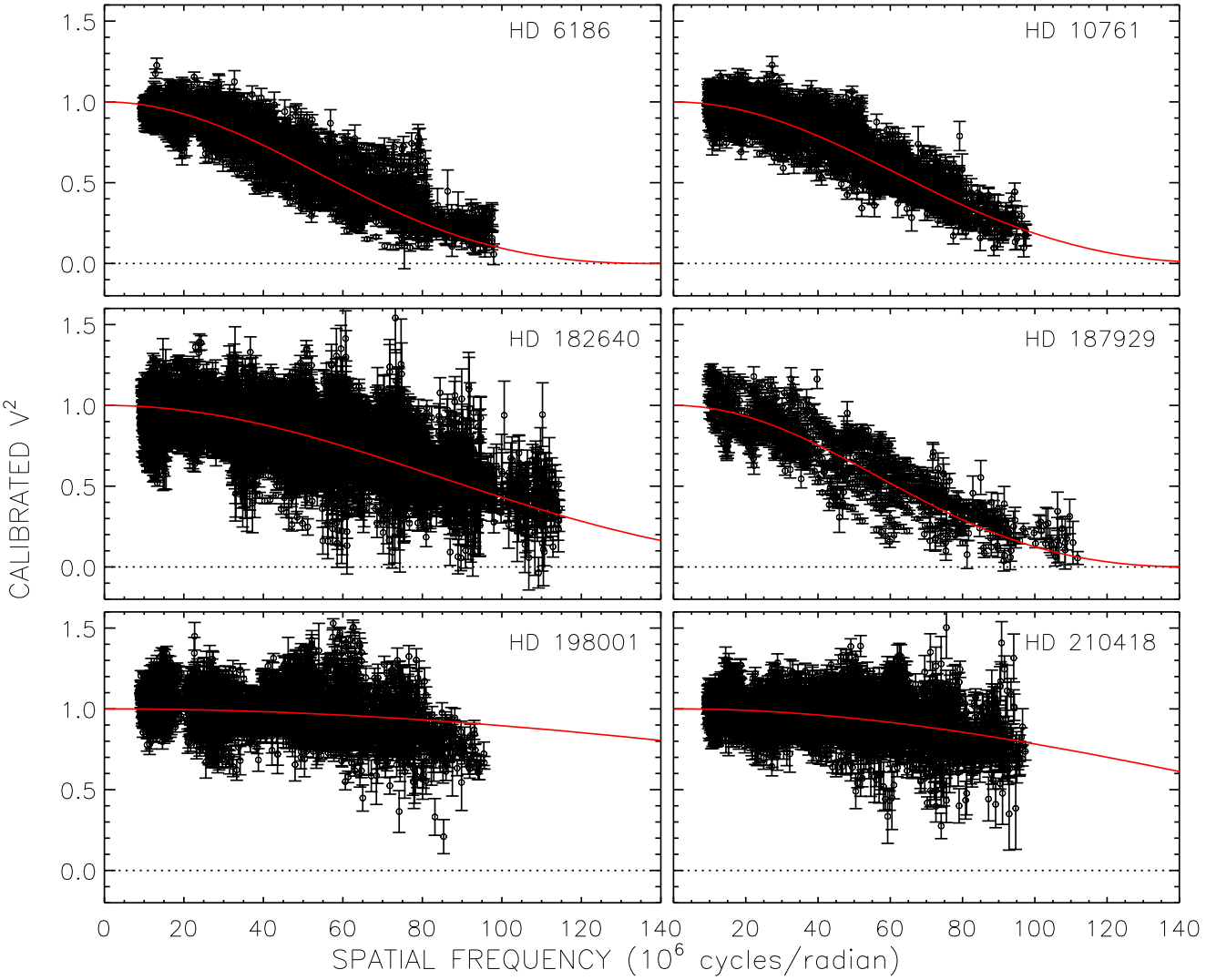

Figure 2. Angular diameter fits to measured visibilities. The solid red line represents the visibility curve for the best-fit $\theta_{\rm LD}$, the open circles are the calibrated visibilities, and the vertical lines are the measurement uncertainties.

Considering that μ_λ is chosen based on a given $T_{\rm eff}$, we used an iterative process to determine the final $\theta_{\rm LD}$. We began with the initial $\theta_{\rm LD}$ determined using the process described in Section 3.1, calculated $T_{\rm eff}$, and used that new $T_{\rm eff}$ to see if μ_λ was altered. The largest change in μ_λ for all the stars was 0.03, which made at most a 0.3% difference in $\theta_{\rm LD}$ (0.004 mas), well within the uncertainty on the diameter. Similarly, $T_{\rm eff}$ changed by a maximum of 11 K as μ_λ was updated. This procedure took one iteration for all the stars to get to the final $\theta_{\rm LD}$, μ_λ, and $T_{\rm eff}$. The initial and final values for all three quantities are listed in Table 5.

4. Discussion and Conclusions

For five of the six stars, the diameter fits are excellent and cover the majority of the visibility curve. The exception is HD 198001/ϵ Aqr. It is the smallest star ever measured with the NPOI at 0.503 mas, and the uncertainty of 0.357 mas is a sizable percentage of that diameter. Still, we find the measurement of value, even as we hope to improve on the uncertainty with future observations.

Two of the stars have been previously measured using interferometry in the last 10 yr: van Belle et al. (2021) determined a diameter of 1.923 ± 0.045 mas for HD 6186/ϵ Psc, compared to our measurement of 1.887 ± 0.025 mas, and Boyajian et al. (2012) found a diameter of 0.862 ± 0.018 mas for HD 210418/θ Peg, versus our 0.688 ± 0.031 mas. Considering this is one of the smallest diameters ever measured with the NPOI and is below the resolution limit, this discrepancy is not surprising.

Interestingly, HD 187929/η Aql was observed using four-way data collection in 2005 (with three siderostats per spectrograph), and Figure 4 shows how the older data compare to the six-way data (with four siderostats per spectrograph). The diameter determined from the 4-way data is 1.804 ± 0.007 mas (Baines et al. 2018), and the diameter from the six-way data is 1.808 ± 0.055 mas. The four-way data show a tighter fit to the visibility curve while the six-way data have more spread around the best-fit angular diameter.

The larger spread in the visibilities and residuals for the six-way data can be attributed to two effects: the reduction of the visibility amplitudes due to flux imbalance, and crosstalk between the different baselines due to nonlinearities in the fast-delay line modulation strokes (Schmitt et al. 2008). In the case of flux imbalance, the V^2 of a baseline observed in a detector that includes multiple siderostats, or a significant amount of

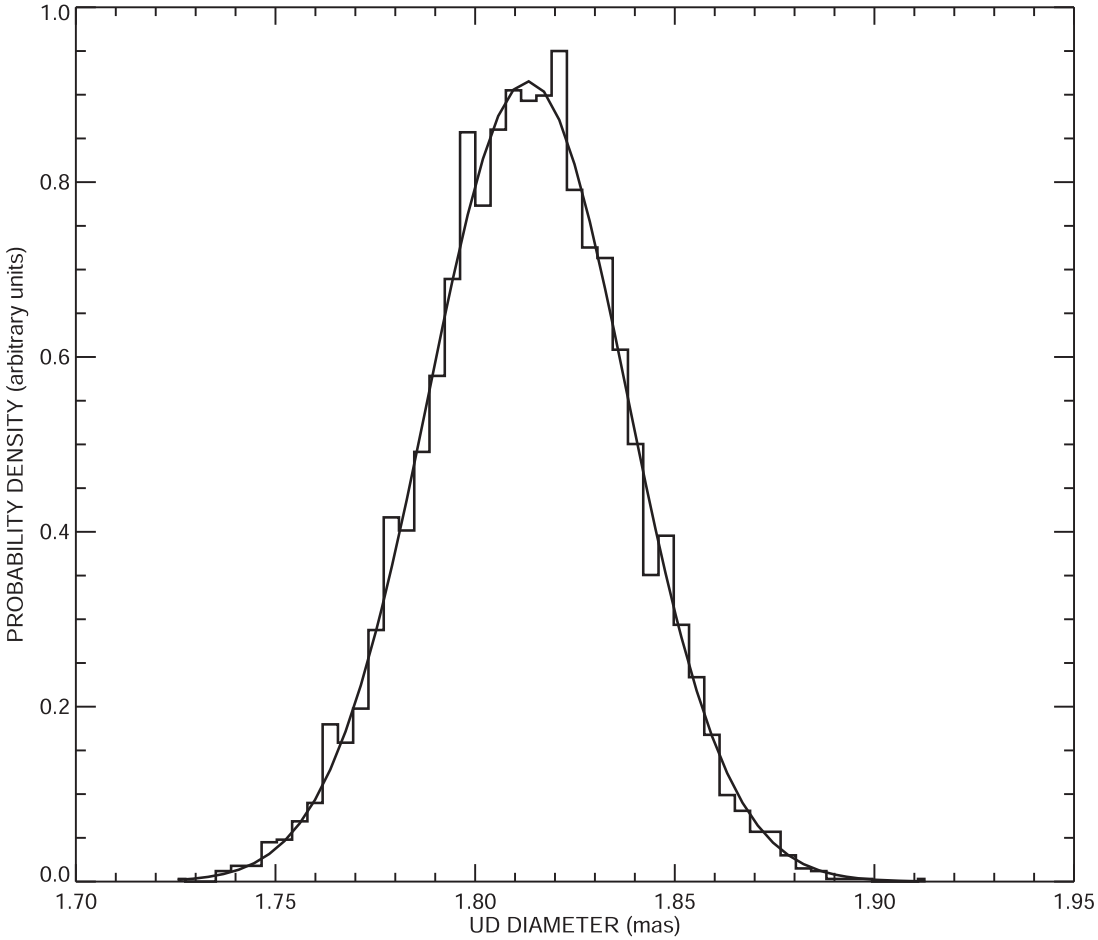

Figure 3. An example probability density solution for the diameter fit to HD 6168/ϵ Psc visibilities as described in Section 3.1.

Table 6
Derived Stellar Parameters

Target HD	Spectral Type	R ($R_\odot$)	σ_R (%)	$F_{\rm BOL}$ (10^{-6} erg s^{-1} cm^{-2})	$A_{\rm V}$ (mag)	$T_{\rm eff}$ (K)	σ_T (%)	L ($L_\odot$)
6186	G9 III-IV	11.39 ± 0.19	1.7	0.648 ± 0.003	0.08 ± 0.01	4834 ± 32	0.7	63.92 ± 1.33
10761	G9 III-IV	14.38 ± 0.21	1.5	0.660 ± 0.003	0.09 ± 0.01	5152 ± 28	0.6	131.50 ± 2.75
182640	F0 IV-V	2.01 ± 0.04	2.0	1.130 ± 0.001	0.00 ± 0.00	6958 ± 46	0.7	8.52 ± 0.26
198001	A0 V	4.05 ± 2.87	71.0	0.920 ± 0.004	0.00 ± 0.00	10221 ± 3627	35.5	161.18 ± 9.04
210418	A3 III-IV	2.01 ± 0.11	5.5	0.961 ± 0.005	0.00 ± 0.00	8835 ± 199	2.3	22.24 ± 1.37

Note. The spectral types are those that provide the best SED fit as described in Section 3.2. The SED fits are also the source of $F_{\rm BOL}$ and $A_{\rm V}$, while the other parameters are derived as described also in Section 3.2. HD 187929/η Aql is not included here due to its nature as a Cepheid variable, and the SED fit required to obtain these parameters is not usable.

background, can be related to the V^2 where only light from two siderostats is observed (V_o^2), using the following expression:

$$V^2 = \frac{4I_1 I_2 V_o^2}{(\sum I_i)^2}. \quad (3)$$

Here I_1 and I_2 are the fluxes from the two siderostats in a given baseline, while the sum in the denominator corresponds to the light from all siderostats and additional background observed in the same detector. Assuming that all siderostats have identical throughput and no additional background, one can calculate that in the case where three and four siderostats are included in the same spectrograph, their observed V^2's are reduced by 4/9 and 1/4, respectively, relative to the case of a single baseline (i.e., 2 siderostats). Because SNR $\propto NV^2$, we would expect a 9/16 reduction in the SNR when going from three to four siderostats in the same spectrograph. This would account for a significant portion of the increased scatter observed in the six-way data presented in Figure 4, which always have four siderostats per spectrograph.

The other significant source of noise in the six-way data is crosstalk between the multiple baselines recorded in the same spectrograph. Due to the fact that the delay from the fast-delay lines is modulated with stroke amplitudes in the range -4–4 μm (Armstrong et al. 1998), nonlinearities in the delay stroke amplitudes cause power from one baseline to spill into other baselines, affecting the fringe amplitudes and phases. Solutions to this problem include the recalibration of the strokes, an upgrade to new piezo electric actuators with longer

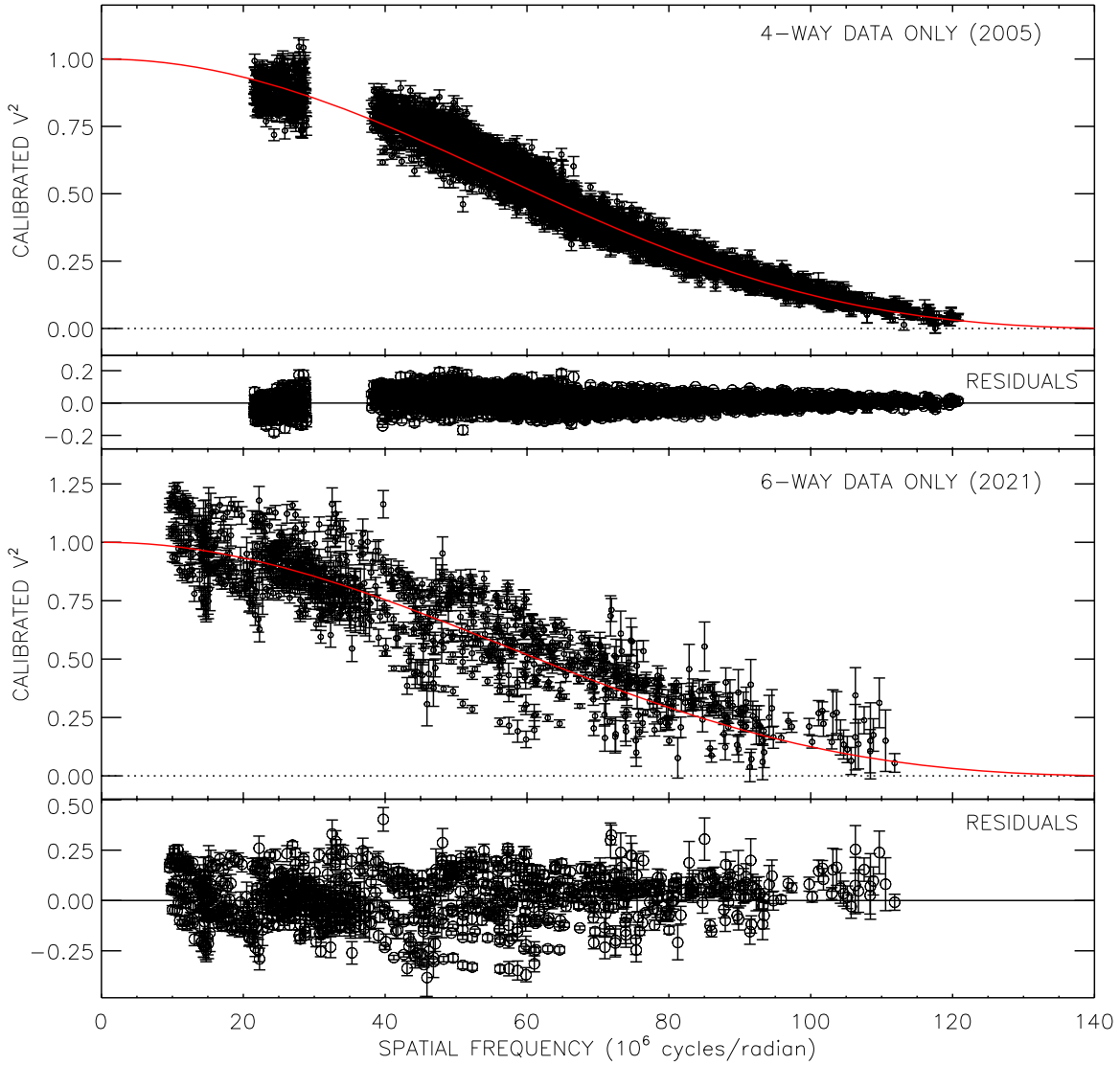

Figure 4. Comparing the angular diameter fit using four-way data (top half) from 2005 with that of six-way data from 2021 (bottom half) for HD 187929/η Aql. The symbols are the same as in Figure 2, while bottom portion of each half shows the residuals to the angular diameter fit. The four-way data had three siderostats per spectrograph, while the six-way data had four siderostats per spectrograph, which partially accounts for the increased scatter in the residuals for the latter.

stroke amplitudes, or to use the VISION beam combiner (Garcia et al. 2016), which does not require the modulation of the delay.

This material is based upon work supported by the National Aeronautics and Space Administration under Grant 18-XRP18_2-0017 issued through the Exoplanets Research Program. The Navy Precision Optical Interferometer is a joint project of the Naval Research Laboratory and the U.S. Naval Observatory, and is funded by the Office of Naval Research and the Oceanographer of the Navy. This research has made use of the SIMBAD database and Vizier catalog access tool, operated at CDS, Strasbourg, France. This work has made use of data from the European Space Agency (ESA) mission Gaia (https://www.cosmos.esa.int/gaia), processed by the Gaia Data Processing and Analysis Consortium (DPAC; https://www.cosmos.esa.int/web/gaia/dpac/consortium). Funding for the DPAC has been provided by national institutions, in particular the institutions participating in the Gaia Multilateral Agreement.

ORCID iDs

Ellyn K. Baines https://orcid.org/0000-0002-5684-3424
Henrique R. Schmitt https://orcid.org/0000-0003-2450-3246

References

Allende Prieto, C., & Lambert, D. L. 1999, A&A, 352, 555
Alonso, A., Arribas, S., & Martinez-Roger, C. 1996, A&AS, 117, 227
Anderson, E., & Francis, C. 2012, AstL, 38, 331
Armstrong, J. T., Mozurkewich, D., Rickard, L. J., et al. 1998, ApJ, 496, 550
Baines, E. K., Armstrong, J. T., Schmitt, H. R., et al. 2018, AJ, 155, 30
Beichman, C. A., Neugebauer, G., Habing, H. J., et al. 1988, 1, Infrared Astronomical Satellite (IRAS) Catalogs and Atlases. Vol. 1: Explanatory Supplement
Benson, J. A., Hummel, C. A., & Mozurkewich, D. 2003, Proc. SPIE, 4838, 358
Boyajian, T. S., McAlister, H. A., van Belle, G., et al. 2012, ApJ, 746, 101
Gaia Collaboration, Brown, A. G. A., Vallenari, A., et al. 2018, A&A, 616, A1
Burnashev, V. I. 1996, yCat, III/126
Cardelli, J. A., Clayton, G. C., & Mathis, J. S. 1989, ApJ, 345, 245
Castelli, F., & Kurucz, R. L. 2003, IAY Symp. 210, Modelling of Stellar Atmospheres (San Francisco, CA: ASP), A20

Claret, A., & Bloemen, S. 2011, A&A, 529, A75
Cohen, M., Wheaton, W. A., & Megeath, S. T. 2003, AJ, 126, 1090
Colina, L., Bohlin, R. C., & Castelli, F. 1996, AJ, 112, 307
Cutri, R. M., Skrutskie, M. F., van Dyk, S., et al. 2003, yCat, II/246
Ducati, J. R. 2002, yCat, II/237
Duvert, G., Young, J., & Hummel, C. A. 2017, A&A, 597, A8
Garcia, E. V., Muterspaugh, M. W., van Belle, G., et al. 2016, PASP, 128, 055004
Gezari, D. Y., Pitts, P. S., & Schmitz, M. 1999, yCat, II/225
Gezari, D. Y., Schmitz, M., Pitts, P. S., & Mead, J. M. 1993, Catalog of Infrared Observations, NASA Reference Publication 1294 (3rd edn.; Greenbelt, MD: NASA)
Glushneva, I. N., Doroshenko, V. T., Fetisova, T. S., et al. 1983, TrSht, 53, 50
Golay, M. 1972, VA, 14, 13
Hanbury Brown, R., Davis, J., Lake, R. J. W., & Thompson, R. J. 1974, MNRAS, 167, 475
Helou, G., & Walker, D. W. 1988, 1, Infrared Astronomical Satellite (IRAS) Catalogs and Atlases, Vol. 7
Høg, E., Fabricius, C., Makarov, V. V., et al. 2000, A&A, 355, L27
Hummel, C. A., Benson, J. A., Hutter, D. J., et al. 2003, AJ, 125, 2630
Hutter, D. J., Zavala, R. T., Tycner, C., et al. 2016, ApJS, 227, 4
Johnson, H. L., & Mitchell, R. I. 1975, RMxAA, 1, 299
Johnson, H. L., Mitchell, R. I., Iriarte, B., & Wisniewski, W. Z. 1966, CoLPL, 4, 99
Jorgensen, A. M., Mozurkewich, D., Murphy, J., et al. 2006, Proc. SPIE, 6268, 62684A
Kharitonov, A. V., Tereshchenko, V. M., & Knjazeva, L. N. 1988, Alma Ata: Nauka, 1988
McDonald, I., Zijlstra, A. A., & Watson, R. A. 2017, MNRAS, 471, 770
Mermilliod, J.-C. 1987, A&AS, 71, 413
Mermilliod, J. C. 2006, yCat, II/168
Mermilliod, J.-C., & Nitschelm, C. 1989, A&AS, 81, 401
Monet, D. G., Levine, S. E., Canzian, B., et al. 2003, AJ, 125, 984
Neckel, T., Klare, G., & Sarcander, M. 1980, BICDS, 19, 61
Oja, T. 1984, A&AS, 57, 357
Oja, T. 1993, A&AS, 100, 591
Pickles, A. J. 1998, PASP, 110, 863
Press, W. H., Teukolsky, S. A., Vetterling, W. T., & Flannery, B. P. 1992, Numerical Recipes in C. The Art of Scientific Computing (2nd ed.; Cambridge: Cambridge Univ. Press), c1992
Prugniel, P., Soubiran, C., Koleva, M., & Le Borgne, D. 2007, arXiv:astro-ph/0703658
Sánchez-Blázquez, P., Peletier, R. F., Jiménez-Vicente, J., et al. 2006, MNRAS, 371, 703
Schmitt, H. R., Armstrong, J. T., Hindsley, R. B., et al. 2008, The Power of Optical/IR Interferometry: Recent Scientific Results and 2nd Generation Instrumentation (Berlin: Springer), 571
Shao, M., & Colavita, M. M. 1992, ARA&A, 30, 457
Smith, B. J., Price, S. D., & Baker, R. I. 2004, ApJS, 154, 673
Tycner, C., Hutter, D. J., & Zavala, R. T. 2010, Proc. SPIE, 7734, 773439
Gaia Collaboration, Vallenari, A., Brown, A. G. A., et al. 2023, A&A, in press
van Belle, G. T., Lane, B. F., Thompson, R. R., et al. 1999, AJ, 117, 521
van Belle, G. T., von Braun, K., Ciardi, D. R., et al. 2021, ApJ, 922, 163
van Leeuwen, F. 2007, A&A, 474, 653
Wall, J. V., & Jenkins, C. R. 2003, Practical Statistics for Astronomers, Cambridge Observing Handbooks for Research Astronomers, Vol. 3. (Cambridge: Cambridge Univ. Press)
Wegner, W. 2003, AN, 324, 219
Wittkowski, M., Hummel, C. A., Johnston, K. J., et al. 2001, A&A, 377, 981
Zorec, J., Cidale, L., Arias, M. L., et al. 2009, A&A, 501, 297